Adsorption of cations at electrochemical interfaces revisited
Supporting Information

Fabiola Domínguez-Flores[1] and Axel Groß[1]

[1]Institute of Theoretical Chemistry, Ulm University, 89081 Ulm, Germany

Contents

1 Bulk-water simulation and analysis **2**
1.1 O-O RDF . . . 2
1.2 H-H RDF . . . 2
1.3 O-H RDF . . . 3

2 Pt(111)-water interface **4**
2.1 Energy stationarity . . . 4

3 Block consistency assessment **5**

4 Density of states of the hydrated metal-ion interfaces **5**
4.1 Calculation and projection . . . 5
4.2 Substrate and ion dependence of the projected states . . . 6
4.3 Relationship to the CDD analysis . . . 7

5 Trajectory based structural analyses **9**
5.1 Sensitivity to the initial ion configuration . . . 9
5.2 Vacuum occupancy and water network isolation . . . 9
5.3 Observed central gap excursions . . . 11
5.4 RDFs and hydration numbers . . . 12
5.5 Ion-metal contact statistics . . . 12
5.6 Surface-normal ion distance $d_{\mathrm{ion-surf}}$ . . . 15

6 Construction of violin plots from DFT-MD trajectories **15**
6.1 Complete ion-metal distance distributions . . . 16

1 Bulk-water simulation and analysis

To establish a structural reference for bulk water, a DFT-MD simulation of bulk liquid water was performed in a periodic cubic cell containing 33 H_2O molecules at ambient density. After 10 ps of equilibration, an approximately 6.5 ps production trajectory was propagated using a time step of 1 fs and divided into three equal temporal blocks. The O-O, O-H, and H-H radial distribution functions (RDFs) were computed for each block using a vectorized minimum image algorithm under full three-dimensional periodic boundary conditions. The block RDFs were directly compared, and mean ± standard deviation (SD) envelopes were evaluated. Statistical uncertainties were estimated using Flyvbjerg-Petersen blocking to account for temporal correlations.[1] Since the cubic cell length is approximately 10 Å, quantitative interpretation of the minimum image RDFs was restricted to $r \lesssim L/2 \approx 5$ Å. The curves are displayed up to 6 Å only to show the complete raw output over the originally sampled range.

1.1 O-O RDF

The O-O RDF exhibits a well defined first peak at $\sim$ 2.7-2.8 Å, corresponding to the hydrogen bonded O-O separation. A minimum near 3.3 Å delineates the first solvation shell. The three block resolved RDFs closely overlap throughout the physically interpretable range (see Fig. 1), and their standard deviation is small relative to the height of the first peak. This agreement supports structural stationarity of the sampled O-O correlations over the production interval.

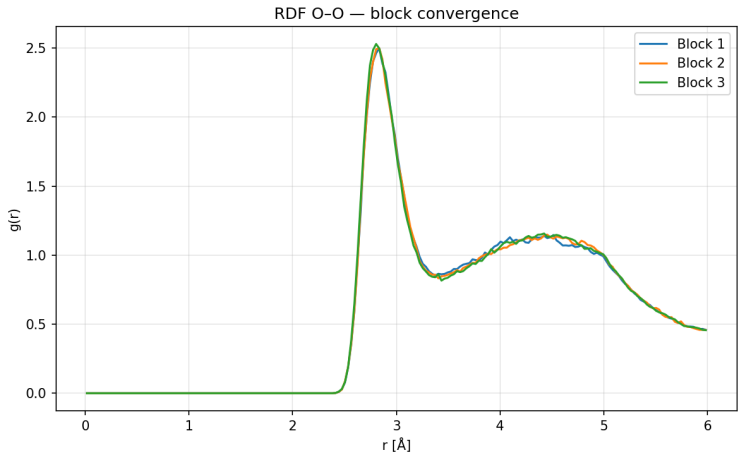


Figure 1: Block resolved O-O RDF for the bulk-water trajectory. Because the cubic cell length is approximately 10 Å, quantitative interpretation is restricted to $r \lesssim L/2 \approx 5$ Å; the portion beyond this range is retained only to display the raw output.

1.2 H-H RDF

The H-H RDF shows the expected intramolecular peak at $\sim$ 1.5 Å, corresponding to the separation between the two hydrogen atoms within a water molecule. Intermolecular

[1] Flyvbjerg, H.; Petersen, H. G. Error estimates on averages of correlated data. *J. Chem. Phys.* **1989**, *91*, 461-466.

correlations appear as broader features between 2.2 and 3.0 Å. As shown in Fig. 2, the three blocks are nearly indistinguishable within statistical noise, indicating stable local water geometry over the sampling window.

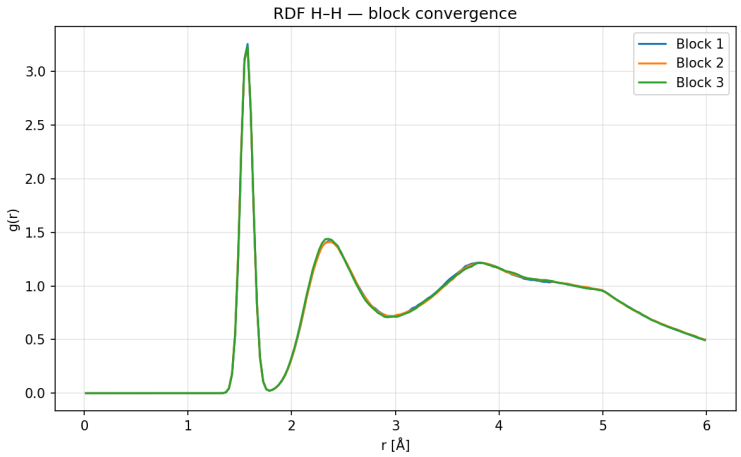


Figure 2: Block resolved H-H RDF for the bulk-water trajectory. Quantitative interpretation is restricted to $r \lesssim L/2 \approx 5$ Å; the portion beyond this range is retained only to display the raw output.

1.3 O-H RDF

The O-H RDF shows two characteristic peaks: (i) a sharp intramolecular O-H peak at ~ 1.0 Å, and (ii) an intermolecular hydrogen bond peak at ~ 1.7-1.9 Å. Both peaks show close agreement across blocks (see Fig. 3), with small variation in height or position within the resolution of the plot. This consistency supports the stationarity of the sampled local O-H structure over the production interval.

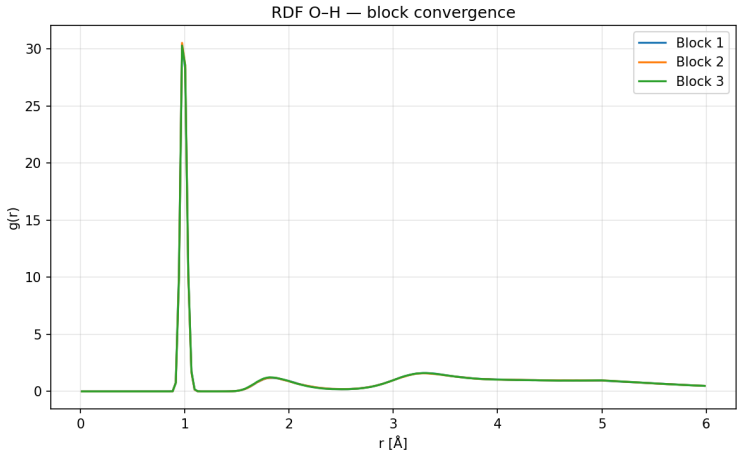


Figure 3: Block resolved O-H RDF for the bulk-water trajectory. Quantitative interpretation is restricted to $r \lesssim L/2 \approx 5$ Å; the portion beyond this range is retained only to display the raw output.

At the mean peak positions, the RDFs show block to block deviations below $\sim 5\%$. The close agreement among the three blocks indicates structural stationarity over the

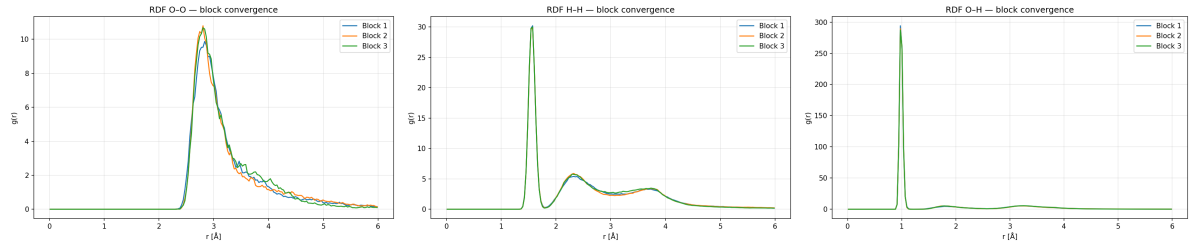
6.5 ps sampling interval. Along with the blocked uncertainty of the mean energy, this provides the bulk internal energy reference $\mu_{H_2O,bulk}(U)$ used in the hydration energy cycles. This block comparison assesses consistency over the sampled interval and is not intended to establish convergence of slower dynamical observables.

2 Pt(111)-water interface

Because the structural relaxation of the metal-water interface is slower than that of the bulk liquid, interfacial water near metal surfaces usually requires a separate block convergence analysis. The same block-resolved analysis was performed for the Pt(111)-water interface. The first peak height of the O-O RDF shows a relative standard deviation of 4.4%, computed using the relative variation.

$$\mathrm{rel}\,\sigma = \frac{\sigma(g_{\mathrm{peak}})}{\langle g_{\mathrm{peak}} \rangle} \tag{1}$$

where $\sigma(g_{\mathrm{peak}})$ is the standard deviation of the first peak height and $\langle g_{\mathrm{peak}} \rangle$ is its block averaged value. Similarly, the maximum of the oxygen z density in the first interfacial layer shows a small block to block relative standard deviation of 2.9%. This metric refers to the peak height of the oxygen density profile, not to an integrated first layer water density. Figure 4 displays the block resolved pair correlations. Since the interfacial water occupies a finite, anisotropic region, its large distance baselines are not interpreted as bulk normalized limits. Instead, the tightly grouped curves are used to diagnose stable local water structure within the system over the analyzed trajectory.



(a) O-O RDF (b) H-H RDF (c) O-H RDF

Figure 4: Block resolved O-O, H-H, and O-H pair correlations for the Pt(111)-water interface. The curves assess consistency of the local interfacial structure across temporal blocks; their large distance baselines are not interpreted as bulk-liquid limits.

2.1 Energy stationarity

The stationarity of the energy observable used in the trajectory averages was assessed by applying block analysis and linear fits to the $E_0(t)$ time series extracted from the output file. Since the simulations were thermostatted in the canonical ensemble, E_0 is not considered as a conserved quantity. The linear fit was used only as a diagnostic of stationarity alongside the block means, not as a test of microcanonical energy conservation or against a universal drift threshold. A representative fit is shown in Fig. 5.

The block mean energy span was computed as $\Delta E_{\mathrm{span}} = \max(E_b) - \min(E_b)$, where E_b is the mean E_0 within temporal block b. This analysis assesses the temporal stability of the sampled mean rather than the convergence of an absolute energy to a unique

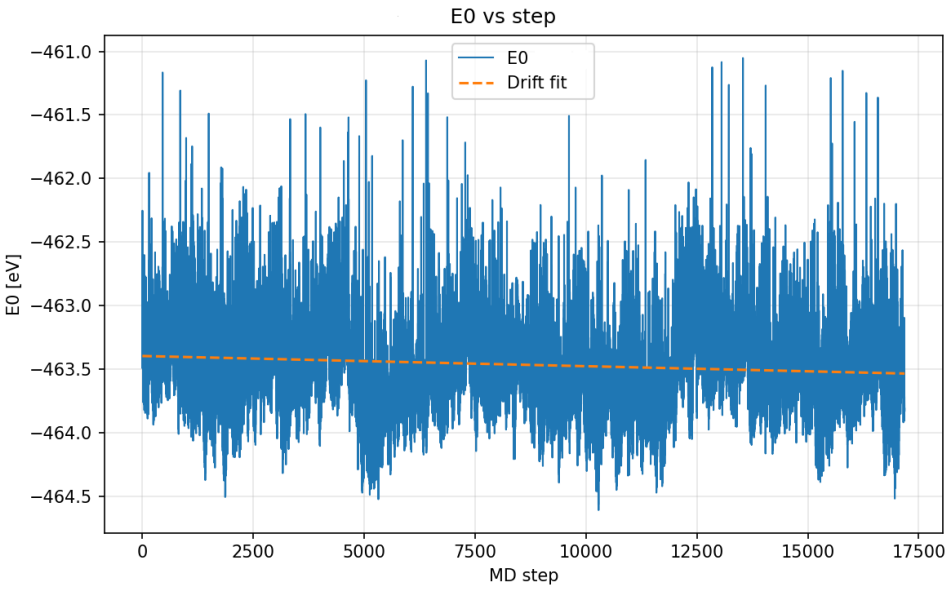


Figure 5: Representative stationarity analysis for the reported E_0 time series of a Pt(111) hydration trajectory. The dashed line is a least-squares fit used together with block averages to identify sustained temporal trends. E_0 is not interpreted as a conserved NVT energy.

value. Block to block variation was incorporated into the uncertainty of relative energy comparisons between hydration states.

Block standard errors were computed from block means chosen to account for temporal correlation in the energy signal. These errors quantify the uncertainty in the mean energy of each hydration state rather than the amplitude of instantaneous fluctuations.

3 Block consistency assessment

For bulk water and the Pt(111)-water reference, variations in the principal structural features between blocks are small, typically below 5%. These results suggest that the local structural descriptors remain stationary over the sampled intervals. However, they do not imply bulk-liquid normalization of the interfacial pair correlations or convergence of dynamical properties on timescales longer than the trajectories.

The energy block analysis provides uncertainty estimates for the mean energies sampled and used to construct ΔU_{step} and $\Delta\Delta U^{\mathrm{ion}}_{\mathrm{step}}$. Accordingly, these analyses support comparisons of internal energy and structural trends within the present model and sampling windows. However, they do not convert those quantities into free energies or address unsampled, long timescale rearrangements.

4 Density of states of the hydrated metal-ion interfaces

4.1 Calculation and projection

The total density of states (DOS) and the atom and orbital projected density of states (PDOS) were evaluated using single point calculations on snapshots extracted from the

analyzed production intervals of trajectories containing seven water molecules per side. Using the highest water coverage for each metal-ion pair allows for a qualitative comparison of ion and substrate dependent electronic features without changing the number of interfacial water molecules simultaneously. The snapshots were selected based on structural criteria to illustrate clear local hydration environments, with water molecules coordinated around the cation. Therefore, the selection was independent of the resulting DOS features. The same snapshot was used for the DOS and the corresponding charge density difference (CDD) map for each system, enabling a comparison of the energy and real space analyses for a configuration matched geometry.

Since the configurations were selected to demonstrate a well defined local hydration structure rather than through an objective ensemble sampling criterion, the spectra and CDD maps should be considered illustrative snapshots rather than averaged trajectory observables. These snapshots are used to interpret electronic redistribution in specific configurations extracted from the analyzed production intervals. Sampled contact fractions, coordination statistics, and other population level conclusions are obtained from the complete DFT-MD trajectories instead.

The single point DOS calculations employed the RPBE functional, PAW potentials, and a plane-wave kinetic energy cutoff of 400 eV, as used during density functional theory molecular dynamics (DFT-MD). The DFT-MD trajectories were performed using a Γ centered $1 \times 1 \times 1$ k-point mesh. The DOS and PDOS were subsequently evaluated through single point calculations on selected trajectory configurations using a denser Γ centered $3 \times 3 \times 1$ k-point mesh to improve Brillouin zone sampling of the electronic states. The atomic geometries were kept fixed during these calculations. Electronic convergence was set to 10^{-6} eV. Gaussian smearing with a width of 0.1 eV was applied. The DOS was sampled on a 2,000 point grid. Site and angular momentum resolved contributions were obtained, using the projector functions supplied by the PAW datasets that yield s-, p-, d-, and, where available, f-resolved contributions for each atom. Finally, non-spherical contributions to the gradient corrections within the PAW spheres were included.

All energies are reported relative to the shifted Fermi energy of $E_{\mathrm{F}} = 0$ eV. In Fig. 6, the total DOS is plotted against the left ordinate, whereas the atom projected orbital contributions are reported per atom against the right ordinate. Consequently, the total and projected curves should not be compared by their plotted heights without accounting for the different ordinate scales.

4.2 Substrate and ion dependence of the projected states

All of the investigated systems have a finite DOS at E_{F}, consistent with metallic character of the Pt, Au, and Ag substrates in the presence of the hydrated cations. The occupied states are dominated by the metal d contribution. For Au and Ag, this contribution is concentrated predominantly below E_{F}, whereas the Pt d-band extends substantially closer to it. This difference establishes the electronic background of the substrate against which the comparatively small ion projected contributions should be interpreted. However, it does not demonstrate direct coupling between the metal d states and a cation.

The monovalent ions contribute little projected weight near E_{F}. Na^+ shows no pronounced ion-centered feature in the low energy unoccupied region on Pt, Au, or Ag. K^+, by contrast, exhibits a clear substrate dependence. The Au-K projected feature is unoccupied and appears near +5.4 eV with a maximum of approximately 0.85-0.90 states $\mathrm{eV}^{-1}\,\mathrm{atom}^{-1}$. The corresponding Ag-K feature reaches approximately

1.1 states $\mathrm{eV}^{-1}\,\mathrm{atom}^{-1}$. The K PDOS on Pt remains nearly featureless over the same energy interval. Thus, the unoccupied K feature is not a universal property of interfacial K^+, but a substrate dependent response observed for the selected Au-K and Ag-K configurations. Because these high lying features are referenced only to E_F and the selected configurations were not aligned to a common vacuum level, their absolute positions cannot be compared directly across substrates. If they lie close to the vacuum level, continuum like states and PAW projection effects may contribute to the projected intensity. The K feature is therefore treated as a high energy projected feature of the selected configurations, not as a robust ion localized state unless vacuum levels or work functions are explicitly verified.

Ca^{2+} produces the most prominent cation projected feature. A strong, predominantly Ca *d* like contribution appears in the unoccupied region, with numerical maxima of approximately 4.6, 3.8-4.0, and 3.4 states $\mathrm{eV}^{-1}\,\mathrm{atom}^{-1}$ for Pt-Ca, Au-Ca, and Ag-Ca, respectively. In the selected configurations, the intensity of this contribution decreases and its position moves towards E_F in the sequence Pt $\rightarrow$ Au $\rightarrow$ Ag, indicating substrate dependent variation in the unoccupied Ca projected response. The Ca maxima quoted here were obtained from the numerical PDOS data. Parts of these peaks exceed the common right-axis range used in the figures below.

This trend should not be interpreted as direct evidence of metal-Ca *d*-state hybridization. In the normalized orbital resolved Pt-Ca spectrum, the Pt *d* contribution decreases close to its unoccupied state baseline before the Ca *d* contribution becomes pronounced. These two contributions show little energetic overlap in the relevant region. Furthermore, since Ca^{2+} is nominally closed shell, the unusually intense and relatively isolated Ca *d* feature must be treated with caution. A contribution from the finite spatial extent and composition dependence of the PAW projector functions cannot be excluded for a cation situated in a heterogeneous metal-water interface environment.

For the Pt-Mg system, the Mg PDOS remains weak and lacks an intense, low-lying unoccupied feature comparable to the Ca feature. This difference is consistent with the distinct interfacial hydration structures of Mg^{2+} and Ca^{2+} reported in the main text, but that structural interpretation is not derived from the PDOS itself. Since Mg^{2+} was not simulated on Au or Ag, no substrate dependent Mg trend can be inferred.

4.3 Relationship to the CDD analysis

As discussed in the main text, the DOS and CDD analyses provide complementary information. The DOS reveals the energy distribution and orbital projection of the electronic states. The CDD maps, on the other hand, illustrate where electron accumulation and depletion occur in real space when the hydrated ion-water complex interacts with the metal. Their comparison is particularly informative for K^+. Although its K PDOS is nearly featureless in the energy region containing the Au-K and Ag-K peaks, Pt-K exhibits an ion-centered dipolar redistribution in the CDD. Therefore, polarization in real space around K^+ does not necessarily produce a distinct, ion-localized DOS feature.

Similarly, the Ca CDD maps reveal significant charge redistribution around the hydrated cation and the metal-water interface in real space. However, the maps do not independently validate the magnitude or d-orbital assignment of the large Ca projected peak. The absence of pronounced Mg or Na projected peaks does not imply an absence of electronic responses, as both ions exhibit localized redistribution in their respective CDD sections.

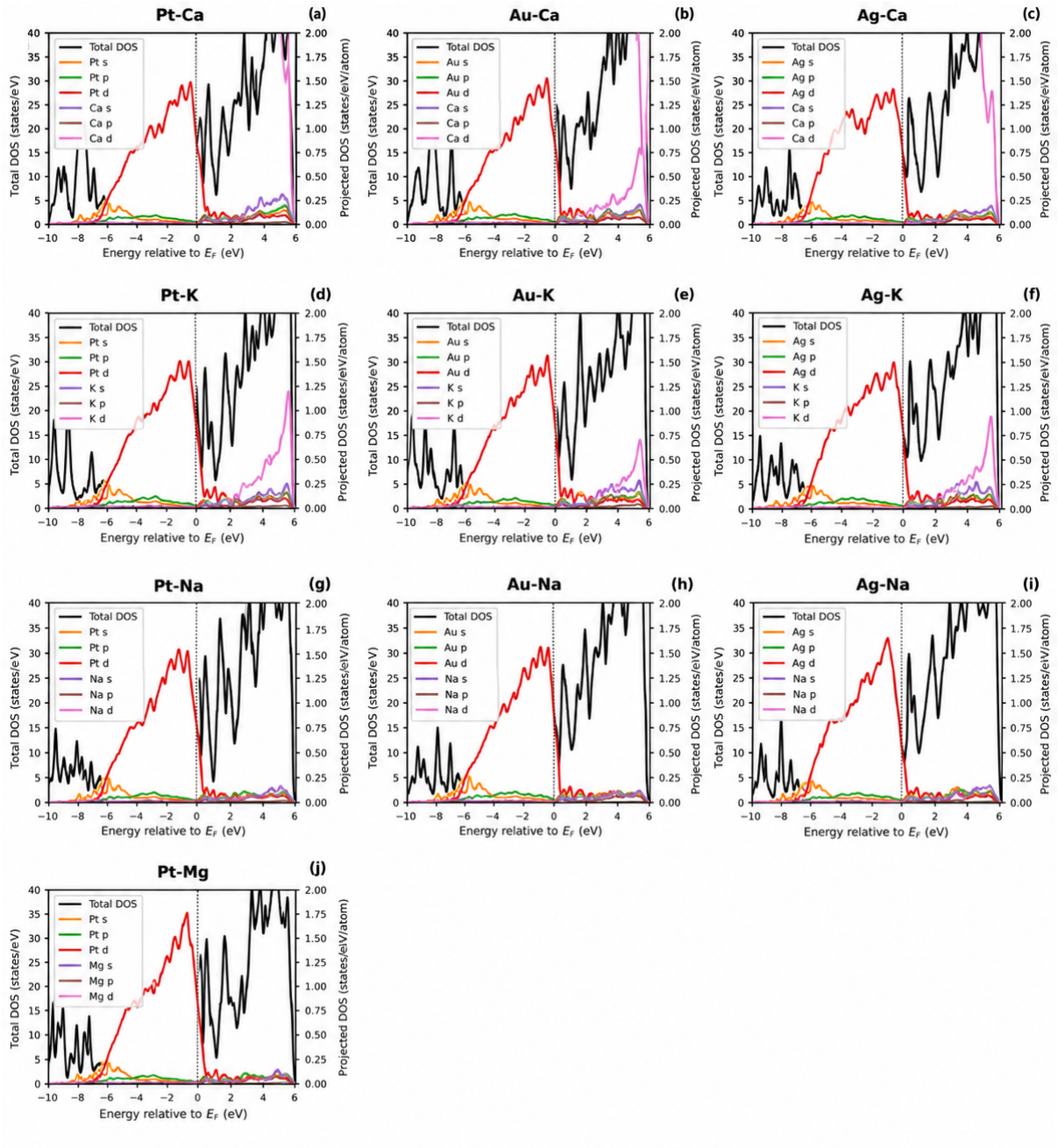


Figure 6: Total, atomic and orbital projected densities of states for hydrated cations at Pt(111), Au(111), and Ag(111): (a) Pt-Ca^{2+}, (b) Au-Ca^{2+}, (c) Ag-Ca^{2+}, (d) Pt-K^{+}, (e) Au-K^{+}, (f) Ag-K^{+}, (g) Pt-Na^{+}, (h) Au-Na^{+}, (i) Ag-Na^{+}, and (j) Pt-Mg^{2+}. The black curve shows the total DOS and uses the left ordinate. The colored curves showing the metal and ion PDOS use the right ordinate and are reported per atom. The vertical dotted line marks the Fermi energy ($E_F = 0$ eV). A common PDOS ordinate is used to facilitate qualitative comparison. The displayed spectra correspond to representative interfacial configurations rather than trajectory averages. For Ca^{2+}, the d projected maxima extend above the displayed PDOS range. The numerical maxima quoted in the text were obtained from the underlying data.

Overall, the results distinguish general interfacial polarization from substrate specific ion projected spectral features. However, the energetic overlap in the PDOS is insufficient to establish covalent bonding. Conversely, the absence of clear overlap does not exclude a weak covalent contribution.

5 Trajectory based structural analyses

5.1 Sensitivity to the initial ion configuration

To examine whether the compact interfacial configurations observed in the original production trajectories depend on the initial placement of the cation, additional DFT-MD simulations were performed using alternative initial geometries. In these calculations, the cation was positioned above the interfacial water layer instead of next to the metal surface so that water would initially occupy the space between the ion and the metal.

The tests included Pt-Mg^{2+}, Pt-Ca^{2+}, Pt-Na^{+}, and Pt-K^{+} with five and seven H_2O molecules per interface, together with Au-Ca^{2+} and Ag-Ca^{2+} with seven H_2O molecules per interface. Alternative trajectories were propagated for at least 20 ps, see Fig. 7. This included an initial 10 ps equilibration period, followed by at least 10 ps of additional MD sampling. Complete trajectories, including initial equilibration periods, were examined to characterize evolution from displaced initial geometries. Subsequent sampling intervals were used to evaluate persistence of resulting interfacial configurations.

Examining the resulting trajectories revealed that the ions shifted from their initial positions to more compact interfacial configurations. The divalent cations exhibited a particularly pronounced approach toward the surface, accompanied by the reorganization or displacement of the initially intervening water molecules. The resulting configurations exhibited short ion-metal separations with no visible water molecules occupying the intervening region.

These observations demonstrate that compact divalent configurations can evolve from initial structures where the ion is separated from the surface by interfacial water. Therefore, these configurations are not solely inherited from the initial contacting geometries used in the original production simulations. However, these tests do not determine equilibrium adsorption free energies, establish unique equilibrium populations, or exclude other metastable configurations.

5.2 Vacuum occupancy and water network isolation

To characterize the movement of water away from metal surfaces and into the central part of the nominal vacuum gap, we conducted a unified post processing analysis of the original production trajectories that were used to generate the structural statistics presented in the main text. For each frame, we defined the instantaneous top and bottom metal reference planes using the mean z positions of the outermost metal layers. We computed the wrapped distance to the nearest metal plane for each water oxygen atom as follows:

$$d_{\mathrm{surf},i} = \min\Big(|z_i - z_{\mathrm{top}}|_{\mathrm{PBC}},\, |z_i - z_{\mathrm{bot}}|_{\mathrm{PBC}}\Big) \tag{2}$$

where z_i is the oxygen coordinate along the surface normal and the wrapped distances are evaluated using periodicity along that direction.

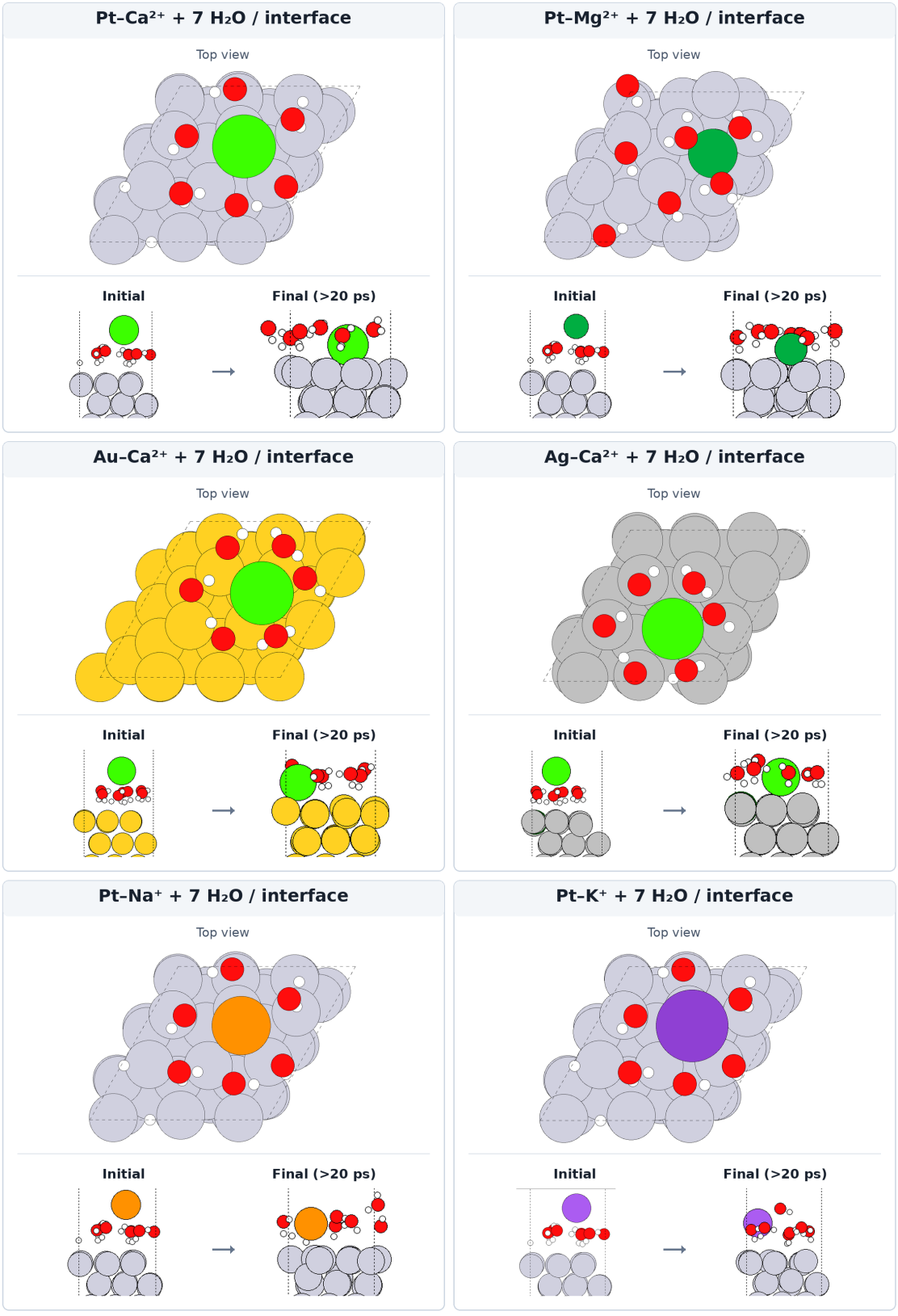


Figure 7: Sensitivity of the interfacial configurations to the initial ion placement. The initial configurations (low-left) and representative configurations obtained after more than 20 ps of DFT-MD (low-right) are shown for Pt-Ca^{2+}, Pt-Mg^{2+}, Au-Ca^{2+}, Ag-Ca^{2+}, Pt-Na^{+}, and Pt-K^{+}, each containing seven H_2O molecules per interface. The alternative configurations were initialized with the cations above the interfacial water layer. The snapshots illustrate the subsequent structural reorganization but do not establish contact fractions, residence times, or equilibrium adsorption populations.

An oxygen is classified as "vacuum-like" if $d_{\mathrm{surf},i} \geq d_{\mathrm{vac}}$, with $d_{\mathrm{vac}} = 6.0$ Å. This criterion identifies excursions into the low-density tail of the interfacial region but does not imply the formation of a true gas phase water molecule.

For each trajectory we constructed two frame resolved time series: (i) a binary indicator of whether any vacuum-like oxygen is present in frame t,

$$I_{\mathrm{vac}}(t) = \begin{cases} 1 & \text{if } \exists\, i \text{ such that } d_{\mathrm{surf},i}(t) \geq d_{\mathrm{vac}} \\ 0 & \text{otherwise,} \end{cases} \tag{3}$$

and (ii) the number of vacuum-like oxygens in that frame, $N_{\mathrm{vac}}(t)$. Their time averages,

$$f_{\mathrm{vac}} = \langle I_{\mathrm{vac}} \rangle, \qquad \bar{N}_{\mathrm{vac}} = \langle N_{\mathrm{vac}} \rangle, \tag{4}$$

quantify, respectively, the fraction of frames containing at least one vacuum-like excursion and the mean number of vacuum-like oxygens per frame.

In addition, we characterized the connectivity of the water network through O-O clustering. Two oxygens were considered connected if their minimum image separation was less than $r_{\mathrm{OO}}^{\mathrm{cut}} = 3.3$ Å. A water molecule was classified as "isolated" if its oxygen belonged to a cluster of size one (i.e., if there were no oxygen neighbors within $r_{\mathrm{OO}}^{\mathrm{cut}}$). Similarly, we defined $I_{\mathrm{iso}}(t)$ (the presence of any isolated water in frame t) and $N_{\mathrm{iso}}(t)$ (the number of isolated water molecules in frame t), and report their averages:

$$f_{\mathrm{iso}} = \langle I_{\mathrm{iso}} \rangle, \qquad \bar{N}_{\mathrm{iso}} = \langle N_{\mathrm{iso}} \rangle \tag{5}$$

These isolation metrics quantify the prevalence of intermittently uncoordinated water molecules anywhere in the simulation cell. These isolation metrics are global quantities. They are not dependent on oxygen satisfying the vacuum-like criterion. Therefore, they cannot determine if a particular vacuum-like molecule is connected to an interfacial water cluster.

5.3 Observed central gap excursions

Table 1 reports the four occupancy and isolation metrics for each metal-ion pair and water coverage. Vacuum-like occupancy is negligible for most hydration states for Ca^{2+} and Mg^{2+} on Pt(111), and for Ca^{2+} on Au(111) and Ag(111), with $\bar{N}_{\mathrm{vac}} \leq 0.042$ except for Pt-Ca^{2+} at $n = 7$, for which $\bar{N}_{\mathrm{vac}} = 0.117$. Thus, under the present operational definition, these systems predominantly retain water within 6 Å of a metal reference plane.

For monovalent ions (Na^+ and K^+), vacuum-like excursions tend to occur more frequently with higher hydration. The most pronounced example is Na^+ on Au(111) with seven water molecules per side, where $\bar{N}_{\mathrm{vac}} = 1.088$ and $f_{\mathrm{vac}} = 0.634 \pm 0.080$. Substantial occupancy is observed for Pt-K^+, Pt-Na^+, Ag-K^+, and Ag-Na^+ at the highest coverage. These values are consistent with more frequent extension of the interfacial water network into the central part of the gap at higher local water availability. However, the operational vacuum-like classification does not imply gas phase evaporation.

Global isolation counts typically decrease as the number of water molecules increases. However, vacuum-like occupancy often increases. This combination is consistent with the formation of more spatially extended water networks at higher coverage. Nevertheless, these two aggregate observables do not identify the connectivity or residence history of the same water molecule. In particular, they cannot distinguish between transient central

gap excursions, transfers between the two periodic interfaces, or cross-gap connections between water clusters.

The analysis provides no evidence that the sampled systems are dominated by a persistent, detached water population. However, the aggregate metrics cannot determine the residence time or connectivity of individual molecules.

5.4 RDFs and hydration numbers

The ion-oxygen radial distribution function, $g_{\mathrm{ion-O}}(r)$, was constructed separately for each metal-ion coverage system. At each saved frame, an ion and the oxygen atoms of the water molecules were assigned to the upper or lower interface relative to the center of the slab. Only ion-oxygen pairs belonging to the same interface were included, and all distances were evaluated using the minimum image convention. Then, equivalent samples from the two interfaces and all analyzed frames were pooled to construct the distributions. Although pooling the two sides increases the number of sampled ion environments, it does not create independent trajectories from the same cell.

The first shell cutoff, $r_{\mathrm{min}}^{\mathrm{ion-O}}$, was defined as the first minimum following the principal peak of the smoothed same-side $g_{\mathrm{ion-O}}(r)$. The smoothing method, its numerical bandwidth or window, and the saved-frame interval must be reported from the actual post processing settings because these choices affect the numerical location of the minimum. For ion i in frame t, the instantaneous hydration number is given by:

$$N_{\mathrm{O},i}(t) = \sum_{o \in O_i^{\mathrm{same\ side}}} \Theta\Big(r_{\mathrm{min}}^{\mathrm{ion-O}} - r_{io}\Big) \tag{6}$$

where r_{io} is the minimum image ion-oxygen distance. The trajectory averaged hydration number reported in the hydration and contact table in the main text is

$$N_{\mathrm{hyd}} = \langle N_{\mathrm{O},i}(t) \rangle_{i,t} \tag{7}$$

where the average gives equal weight to ion samples from the upper and lower interfaces. The quantity n_1 is the most probable integer value, or mode, of the corresponding instantaneous first shell coordination number distribution. It is not a second independently averaged coordination number.

We evaluated the same side ion-metal distance distributions separately, using only the atoms in the outermost metal layer at the interface containing the ion. The first short distance peak of this distribution supplied $r_{\mathrm{peak}}^{\mathrm{ion-M}}$, which was used to construct the distance cutoff defined below. The ion-metal RDF alone was not used to classify contact because the final criterion requires that no water oxygen be interposed between the ion and the metal surface.

5.5 Ion-metal contact statistics

Contact was evaluated independently for each ion relative to the outermost metal layer on the same side of the symmetric slab. For the ion i, the nearest three-dimensional distance to that layer was defined as:

$$d_{\mathrm{ion-M},i}(t) = \min_{j \in S_s} r_{ij} \tag{8}$$

where S_s is the set of surface-metal atoms at the upper or lower interface containing the ion. For each metal-ion system, the distance component of the direct contact cutoff was

Table 1: Vacuum occupancy and global isolation metrics for all metal-ion systems containing 5-7 H_2O molecules per interface. Blocking uncertainties are shown for the fractional occupancies f_{vac} and f_{iso}; $\bar{N}_{\mathrm{vac}}$ and $\bar{N}_{\mathrm{iso}}$ are reported as trajectory averaged counts. Entries reported as zero indicate that no corresponding events were observed during the sampled trajectory; they do not imply an exact physical probability of zero.

System	n **(H_2O)**	$f_{\mathbf{vac}}$	$\bar{N}_{\mathbf{vac}}$	$f_{\mathbf{iso}}$	$\bar{N}_{\mathbf{iso}}$
Pt(111)					
Ca^{2+}	5	0.0000 ± 0.0000	0.000	0.5494 ± 0.0261	0.680
	6	0.0151 ± 0.0083	0.015	0.1039 ± 0.0180	0.109
	7	0.1165 ± 0.0415	0.117	0.0141 ± 0.0056	0.014
K^+	5	0.0225 ± 0.0117	0.028	0.6373 ± 0.0311	1.042
	6	0.0897 ± 0.0206	0.092	0.3237 ± 0.0274	0.384
	7	0.6233 ± 0.0588	0.829	0.3199 ± 0.0334	0.385
Mg^{2+}	5	0.0000 ± 0.0000	0.000	0.0629 ± 0.0091	0.064
	6	0.0146 ± 0.0148	0.015	0.0352 ± 0.0087	0.036
	7	0.0000 ± 0.0000	0.000	0.0018 ± 0.0013	0.002
Na^+	5	0.0630 ± 0.0305	0.064	0.6292 ± 0.0369	0.943
	6	0.0175 ± 0.0087	0.017	0.2914 ± 0.0308	0.324
	7	0.4381 ± 0.0825	0.459	0.1601 ± 0.0289	0.167
Au(111)					
Ca^{2+}	5	0.0000 ± 0.0000	0.000	0.6565 ± 0.0185	0.952
	6	0.0000 ± 0.0000	0.000	0.3269 ± 0.0275	0.365
	7	0.0004 ± 0.0004	0.000	0.0149 ± 0.0034	0.015
K^+	5	0.0166 ± 0.0094	0.017	0.5983 ± 0.0520	0.932
	6	0.1984 ± 0.0405	0.206	0.3699 ± 0.0252	0.434
	7	0.2737 ± 0.0590	0.307	0.1432 ± 0.0265	0.158
Na^+	5	0.1331 ± 0.0437	0.150	0.7013 ± 0.0330	1.119
	6	0.3613 ± 0.0634	0.425	0.4908 ± 0.0287	0.615
	7	0.6338 ± 0.0797	1.088	0.2547 ± 0.0446	0.307
Ag(111)					
Ca^{2+}	5	0.0000 ± 0.0000	0.000	0.6766 ± 0.0156	1.004
	6	0.0001 ± 0.0001	0.000	0.3294 ± 0.0249	0.361
	7	0.0405 ± 0.0229	0.042	0.0641 ± 0.0153	0.067
K^+	5	0.0203 ± 0.0073	0.020	0.5739 ± 0.0397	0.845
	6	0.1223 ± 0.0266	0.128	0.3012 ± 0.0410	0.346
	7	0.5180 ± 0.0472	0.625	0.2151 ± 0.0182	0.246
Na^+	5	0.0314 ± 0.0156	0.031	0.6902 ± 0.0314	1.077
	6	0.1762 ± 0.0725	0.240	0.3589 ± 0.0365	0.431
	7	0.5250 ± 0.0995	0.874	0.2012 ± 0.0342	0.223

constructed from the first peak of the surface restricted, same side ion-metal distance distribution:

$$r_{\mathrm{c},i}^{\mathrm{ion-M}} = \min\left(r_{\mathrm{peak}}^{\mathrm{ion-M}} + \Delta_i, r_{\mathrm{cap},i}\right). \tag{9}$$

The ion-specific increments and upper caps are listed in Table 2. These values were held constant for a given ion across the three substrates and all water coverages. Since $r_{\mathrm{peak}}^{\mathrm{ion-M}}$ is obtained for each metal-ion system, the resulting numerical cutoff may retain a metal dependence even though the ion-specific parameters Δ_i and $r_{\mathrm{cap},i}$ are held constant. The caps prevent the broad first ion-metal shells of larger monovalent ions from being entirely classified as direct contact. When active, the caps deliberately select the short distance portion of the first distribution.

Table 2: Ion-specific parameters used to construct the direct ion-surface contact cutoff in Eq. 9.

Ion	Δ_i / Å	$r_{\mathrm{cap},i}$ / Å
Mg^{2+}	0.25	3.25
Ca^{2+}	0.25	3.55
Na^{+}	0.20	3.35
K^{+}	0.20	3.65

A configuration was classified as direct contact only if two conditions were met simultaneously: (i) $d_{\mathrm{ion-M},i}(t) \leq r_{\mathrm{c},i}^{\mathrm{ion-M}}$ and (ii) no water oxygen was interposed between the ion and its same-side metal surface. Water interposition was tested inside a cylinder with a radius of $R_{\mathrm{cyl}} = 3.0$ Å, centered on the lateral projection of the ion and oriented along the slab normal. At the upper interface, oxygen interposition occurred when its lateral minimum image separation from the ion was below R_{cyl} and its vertical coordinate lay between the upper surface plane and $z_{\mathrm{ion}} - \delta_z$. The reverse condition was applied at the lower interface. A tolerance of $\delta_z = 0.15$ Å excluded oxygen atoms lying essentially at the same height as the ion.

No water molecule satisfied the interposition criterion in any of the analyzed frames of the original production trajectories used to calculate the contact statistics. Consequently, for those trajectories, $\chi_{\mathrm{cont},i}(t)$ was determined by the ion-metal distance condition. The interposition test was retained as a conservative component of the general contact definition. Thus, while 'water separated' configurations are part of the general classification scheme, this category was not observed in the sampled trajectories. All sampled non-contact configurations failed the ion-metal distance condition rather than the water interposition condition.

The resulting per-ion indicator was

$$\chi_{\mathrm{cont},i}(t) = \begin{cases} 1, & \text{if the distance condition is satisfied and no water oxygen is interposed,} \\ 0, & \text{otherwise.} \end{cases} \tag{10}$$

The sampled contact fraction reported in the hydration and contact table in the main text is the average over ion samples from both interfaces and all analyzed frames,

$$f_{\mathrm{cont}} = \langle \chi_{\mathrm{cont},i}(t) \rangle_{i,t}. \tag{11}$$

Therefore, it is a finite, per-ion structural descriptor of the trajectory, not an equilibrium probability or the fraction of frames in which at least one of the two ions in the simulation cell is in contact.

The instantaneous contact count was used to characterize the local multiplicity of a contact without including more distant atoms from a broad first surface shell:

$$n_{c,i}(t) = \chi_{\mathrm{cont},i}(t) \sum_{j \in S_s} \Theta\Big(r_{\mathrm{c},i}^{\mathrm{ion-M}} - r_{ij}\Big)\, \Theta(d_{\mathrm{ion-M},i}(t) + \delta_r - r_{ij}) \tag{12}$$

with $\delta_r = 0.25$ Å. Its trajectory average, $\langle n_c \rangle = \langle n_{c,i}(t) \rangle_{i,t}$, includes $n_c = 0$ for every non-contact sample. By contrast:

$$\Big\langle N_M^{\mathrm{cont}} \Big\rangle = \langle n_c \mid \chi_{\mathrm{cont}} = 1 \rangle \tag{13}$$

is the conditional mean number of contacted surface-metal atoms evaluated only when contact is present. The quantities obey the following:

$$\langle n_c \rangle = f_{\mathrm{cont}} \Big\langle N_M^{\mathrm{cont}} \Big\rangle \tag{14}$$

Thus, f_{cont} measures the fraction of sampled direct contact configurations. The trajectory averaged contact count per ion, denoted by $\langle n_c \rangle$ is an unconditional average that includes $n_c = 0$ for non-contact configurations, whereas $\langle N_M^{\mathrm{cont}} \rangle$ describes the local surface coordination conditional on direct contact. However, these operational geometric quantities do not establish a particular electronic bond order or charge transfer mechanism on their own.

5.6 Surface-normal ion distance $d_{\mathrm{ion-surf}}$

The surface-normal ion distance was evaluated separately at each interface. In each frame, the upper and lower surface planes were defined by the mean z coordinates of the atoms in the outermost metal layers. For an ion assigned to the upper or lower interface:

$$d_{\mathrm{ion-surf},i}(t) = \begin{cases} z_i(t) - z_{\mathrm{surf}}^{\mathrm{top}}(t), & \text{upper interface,} \\ z_{\mathrm{surf}}^{\mathrm{bottom}}(t) - z_i(t), & \text{lower interface.} \end{cases} \tag{15}$$

The value reported in the hydration and contact table in the main text is the trajectory mean over equally weighted ion samples from both interfaces. This quantity measures displacement normal to the mean outermost metal plane and differs from the distance between the nearest ion and metal, $d_{\mathrm{ion-M}}$. The latter depends on both lateral registry and the instantaneous vertical position of the nearest surface atom. Consequently, no strict ordering is imposed between the two quantities for the thermally corrugated mobile surface layer. The surface-normal distance is used to characterize vertical localization, but not to assign direct contact by itself.

6 Construction of violin plots from DFT-MD trajectories

Violin plots were used to show the distributions of structural observables that were derived from equilibrated DFT-MD trajectories. Each violin plot visualizes a continuous probability density reconstructed from the saved trajectory samples using a Gaussian kernel

density estimate, with the bandwidth selected by Scott's rule, for which the bandwidth factor scales as $N^{-1/5}$.

All saved frames used in the structural analysis entered the KDE. Because temporally correlated frames are not statistically independent, the KDE bandwidth and the plotted violin shape should be interpreted as descriptive visualization choices rather than as uncertainty estimates. The violin widths were normalized independently for each distribution, so widths should not be compared quantitatively across different systems or panels. In each violin plot, the central horizontal line denotes the median, the colored marker denotes the mean, and the whiskers indicate the sampled minimum and maximum. Since extrema depend on trajectory length, comparisons among systems should emphasize the distribution shape, central tendency, and tails rather than the whisker endpoints alone.

6.1 Complete ion-metal distance distributions

We characterized the dynamic adsorption behavior by analyzing the full distributions of the instantaneous ion-metal distance, $d_{\text{ion-M}}$, which is defined as the shortest three-dimensional distance between a cation and an atom in the outermost, same-side metal layer. Unlike a single time averaged parameter, these distributions (Fig. 8) reveal the relative populations of short and long distance geometries. These distributions reveal shoulders, skewness, and tails associated with minority populations and intermittent excursions between contact-like and more vertically displaced non-contact configurations.

The $d_{\text{ion-M}}$ and the tabulated $d_{\text{ion}-\text{surf}}$ exhibit similar trends, but they are not equivalent. The former represents the full three-dimensional distance to the nearest surface atom, while the latter represents the surface-normal displacement from the mean metal plane. Their relationship depends on lateral registry and corrugation. Violin plots capture the distance component of the operational contact definition. Although that definition also includes a water interposition test, no interposition events were observed in the analyzed trajectories.

Divalent ions exhibit the most persistent short distance populations. The Mg^{2+} on Pt(111) distributions are narrow, with trajectory means of 2.69-2.73 Å across coverages. They show only slightly longer upper tails at 6-7 H_2O. The sampled contact fraction stays near unity throughout, so increasing local water loading primarily changes fluctuations around the dominant sampled contact regime. Similarly, Ca^{2+} retains a dominant short distance population on all three metals: trajectory means of 2.94-3.02 Å on Pt(111), 2.95-3.00 Å on Au(111), and a slight outward shift to 3.02-3.06 Å on Ag(111). These distributions are the broadest among the divalent-ion distributions (upper tails reaching $\sim$ 3.6 Å at 7 H_2O). The sampled contact fraction remains high on every substrate and coverage. Thus, the extended tails reflect excursions around a contacting configuration rather than a shift toward predominantly non-contact adsorption at larger ion-metal distances.

Monovalent ions show broader distributions and a stronger dependence on coverage and substrate. The Na^+ on Pt(111) shifts outward progressively (3.20 $\rightarrow$ 3.30 $\rightarrow$ 3.39 Å for 5 $\rightarrow$ 6 $\rightarrow$ 7 H_2O), with a pronounced tail extending to $\sim$ 5.0 Å at 7 H_2O; f_{cont} drops from 0.720 to 0.464 and then shows a modest apparent recovery to 0.510. Without block uncertainties, this change should be interpreted cautiously. The mean distance alone cannot explain this apparent partial recovery; it instead suggests a redistribution between short range configurations and increasingly prominent long distance excursions.

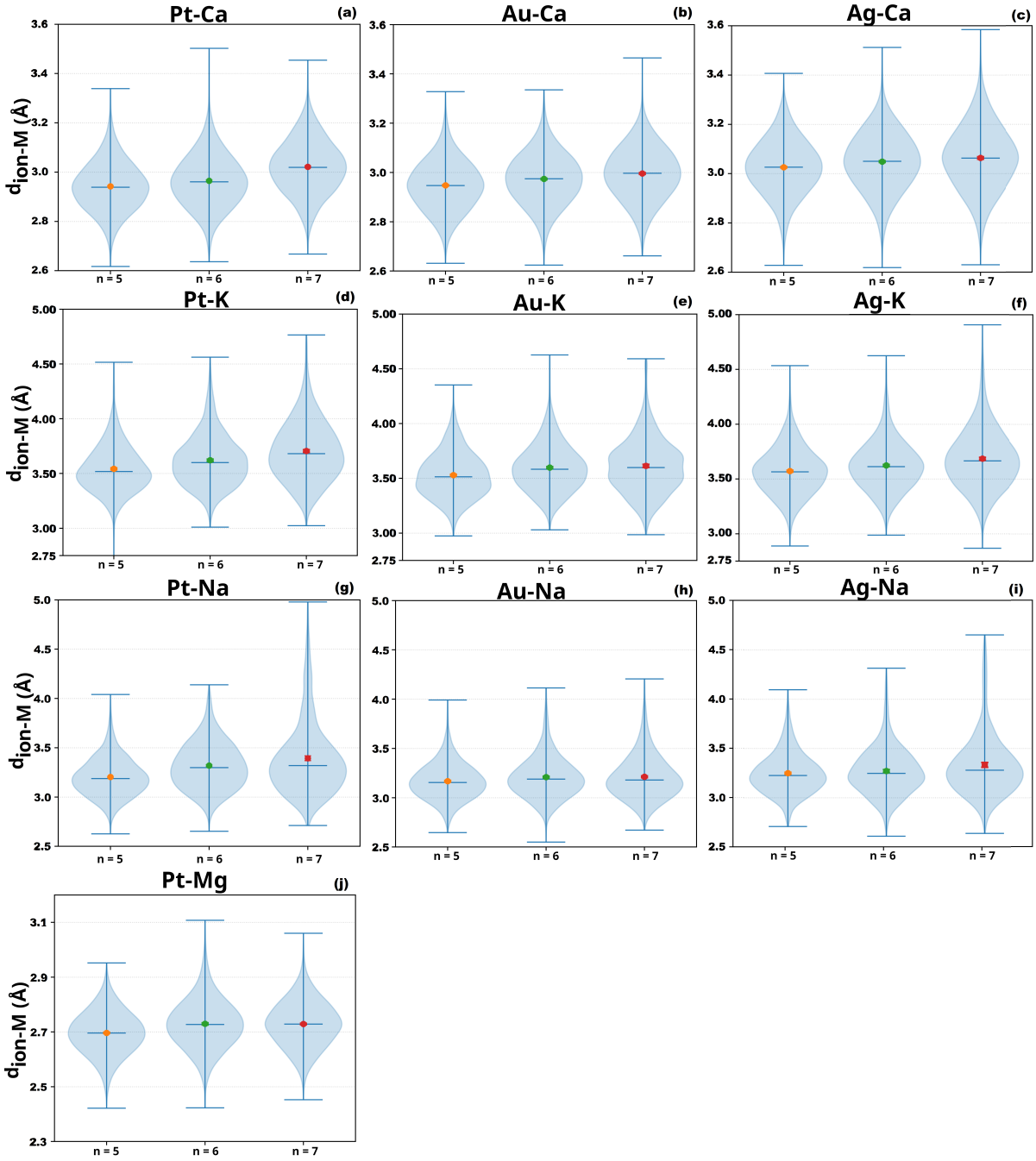


Figure 8: Distributions of the instantaneous ion-metal distance, $d_{\text{ion-M}}$, for hydrated cations at the investigated metal-water interfaces. The panels depict Ca^{2+} on Pt(111), Au(111), and Ag(111); K^{+} on Pt(111), Au(111), and Ag(111); Na^{+} on Pt(111), Au(111), and Ag(111); and Mg^{2+} on Pt(111). Each violin reports the distribution obtained with five, six and seven water molecules per interface. The normalized width of each violin represents the shape of the sampled distance distribution and is not quantitatively comparable across panels. The central horizontal line denotes the median, the colored marker denotes the mean, and the whiskers indicate the sampled minimum and maximum. Mg^{2+} was not simulated on Au(111) or Ag(111). The vertical-axis limits differ among ion groups to display the relevant distance ranges.

The Na^{+} on Au(111) remains comparatively compact (3.15-3.20 Å) with only mild tail lengthening. This is consistent with high and comparatively stable f_{cont} values (0.842, 0.770, 0.743). Na^{+}/Ag(111) shifts from 3.23 to 3.33 Å with tails extending to $\sim$ 4.6 Å,

alongside a gradual decline in f_{cont} (0.694 → 0.633 → 0.571). Thus, Au(111) supports the most persistent short distance population, Ag(111) permits larger outward fluctuations, and Pt(111) shows the strongest apparent non-monotonic contact response.

K^+ exhibits the broadest distributions and the weakest short distance population. The trajectory means increase with hydration on all substrates: Pt(111) 3.53 → 3.60 → 3.70 Å; Au(111) 3.52 → 3.58 → 3.60 Å; Ag(111) increases from 3.56 to 3.67 Å (tail to ∼ 4.9 Å). This parallels the monotonic decrease in f_{cont}: Pt(111) 0.554 → 0.334 → 0.296; Au(111) 0.480 → 0.366 → 0.337; Ag(111) 0.440 → 0.393 → 0.306. However, the coverage interval driving the largest decrease is metal dependent. At 5 H_2O, contact and non-contact populations are substantial, but at $n = 7$, longer distance configurations dominate.

Overall, substrate effects are ion specific rather than following a universal trend. Ca^{2+} retains similar trajectory means but broadens on Ag(111); Na^+ is most compact on Au(111), broadens and shifts outward on Ag(111), and restructures most strongly on Pt(111); K^+ shows comparable trajectory means across metals but differing tail behavior. Narrow distributions with short trajectory mean distances accompany high f_{cont} for divalent ions, while broader, longer tailed distributions reflect greater non-contact sampling for monovalent ions. Although the operational contact definition includes a water interposition test, no interposition events were observed in the original production trajectories used for the contact statistics. The observed variation in f_{cont} is therefore governed by the ion-metal distance condition.